Electronic Supplementary Information (ESI)

Ordered-vacancy-enabled indium sulphide printed in wafer scale with enhanced electron mobility

Azmira Jannat[a†], Qifeng Yao[b†], Ali Zavabeti[c,f*], Nitu Syed[a], Bao Yue Zhang[a], Taimur Ahmed[a], Sruthi Kuriakose[a], Md Mohiuddin[a], Naresh Pillai[a], Farjana Haque[a], Guanghui Ren[a], De Ming Zhu[d], Ningyan Cheng[e], Yi Du[e], Sherif Abdulkader Tawfik[f], Michelle J.S. Spencer[f], Billy Murdoch[f], Lan Wang[f], Chris F. McConville[f], Sumeet Walia[a*], Torben Daeneke[a], Lianqing Zhu[g], Jian Zhen Ou[a*].

[a]School of Engineering, RMIT University, Melbourne, Victoria 3000, Australia

[b]Department of Quantum Materials and Device, Beijing Academy of Quantum Information Sciences, 100193, Beijing, China

[c]College of Materials Science and Technology, Nanjing University of Aeronautics and Astronautics, 29 Jiangjun Ave., Nanjing 211100, Jiangsu, China

[d]Faculty of Science, Engineering and Technology, Swinburne University of Technology, Melbourne, Victoria 3122, Australia

[e]Institute for Superconducting & Electronic Materials, University of Wollongong, Wollongong, New South Wales 2522, Australia

[f]School of Science, RMIT University, Melbourne, Victoria 3000, Australia

[g]Beijing Laboratory of Optical Fibre Sensing and System, Beijing Information Science & Technology, Beijing 100016, China

*E-mail: jianzhen.ou@rmit.edu.au, sumeet.walia@rmit.edu.au, ali.zavabeti@nuaa.edu.cn

† The authors contribute equally in the paper

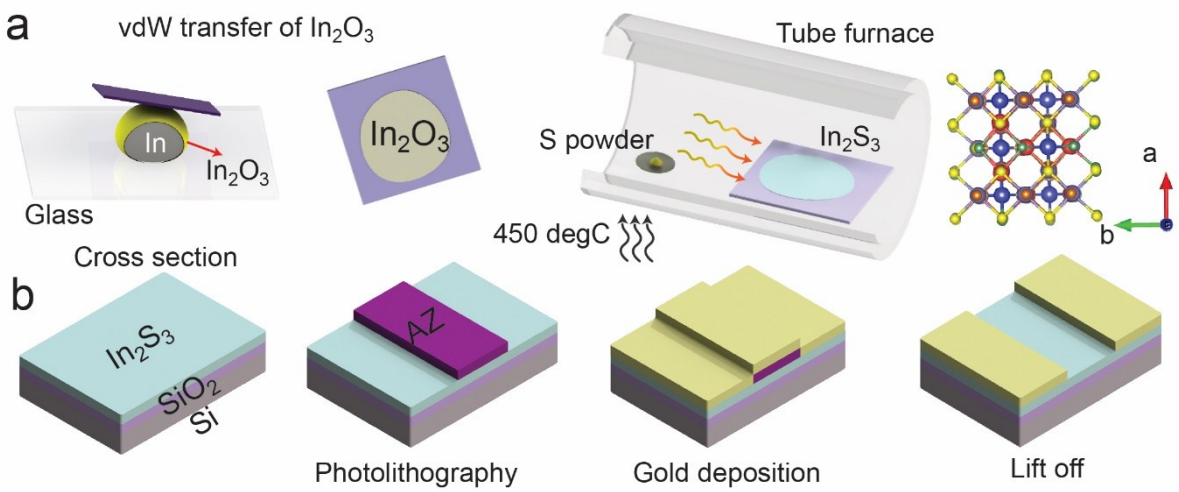

Fig. S1 (a) Synthesis process of single unit-cell-thick tetragonal In_2S_3, (b) Fabrication process of a back-gate field effect transistor based on tetragonal In_2S_3 on the SiO_2/Si substrate.

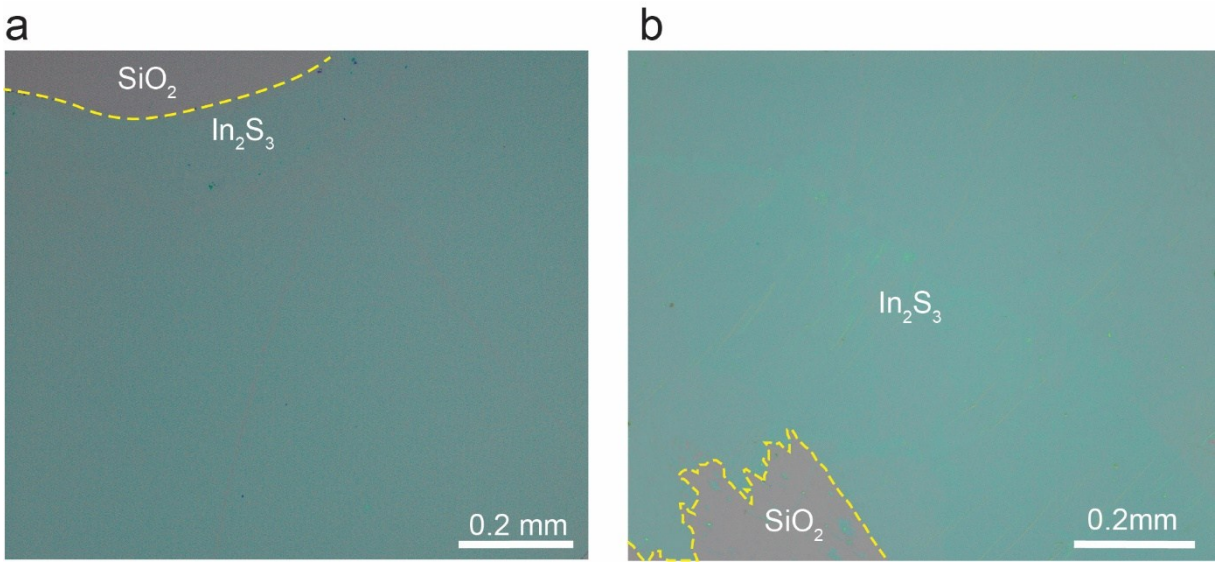

Fig. S2 (a and b) Optical images of synthesised In_2S_3 film showing high degrees of homogeneity featuring.

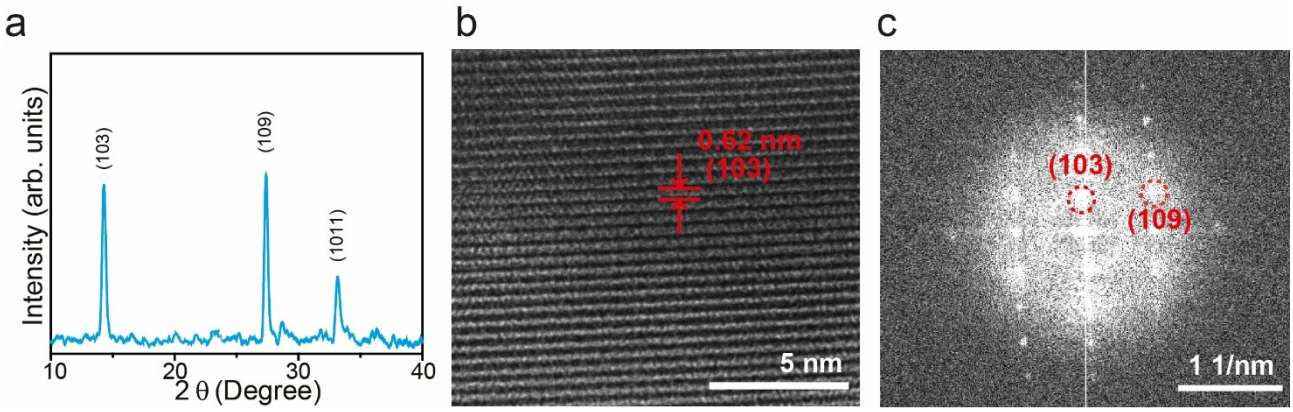

Fig. S3 (a) X-Ray diffraction (XRD) patterns of tetragonal In_2S_3 layer on glass substrates after multiple printing to gain sufficient signal. (b) High resolution transmission electron microscopic (HRTEM) image of tetragonal In_2S_3 sheets featuring high quality fully crystalline layers and (c) corresponding FFT image showing the crystal plane of (103) and (109).

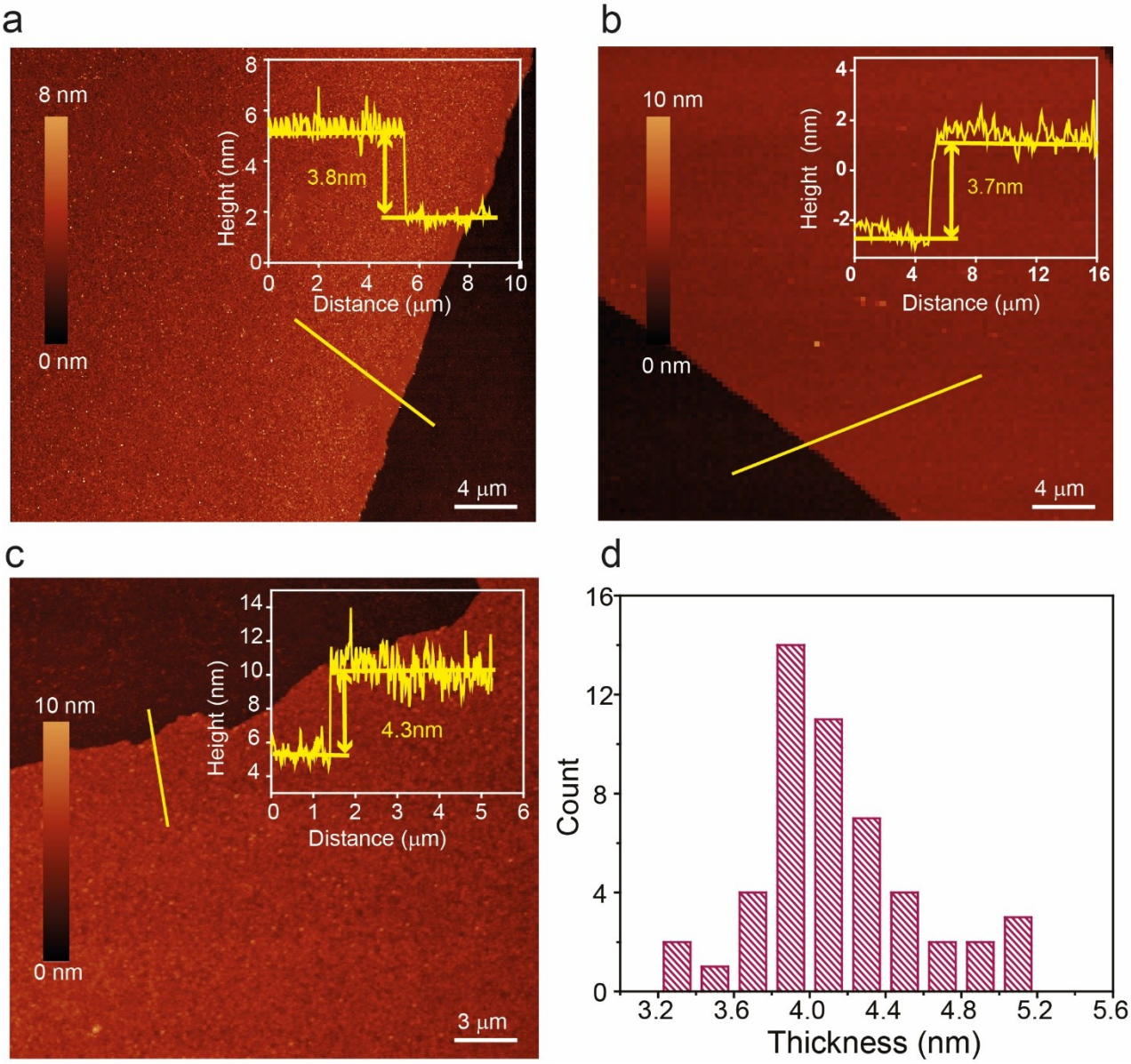

Fig. S4 (a, b and c) AFM images of In_2S_3 layers with corresponding height profiles (inset). (d) Statistical distribution of the thicknesses of In_2S_3 layers over 50 samples.

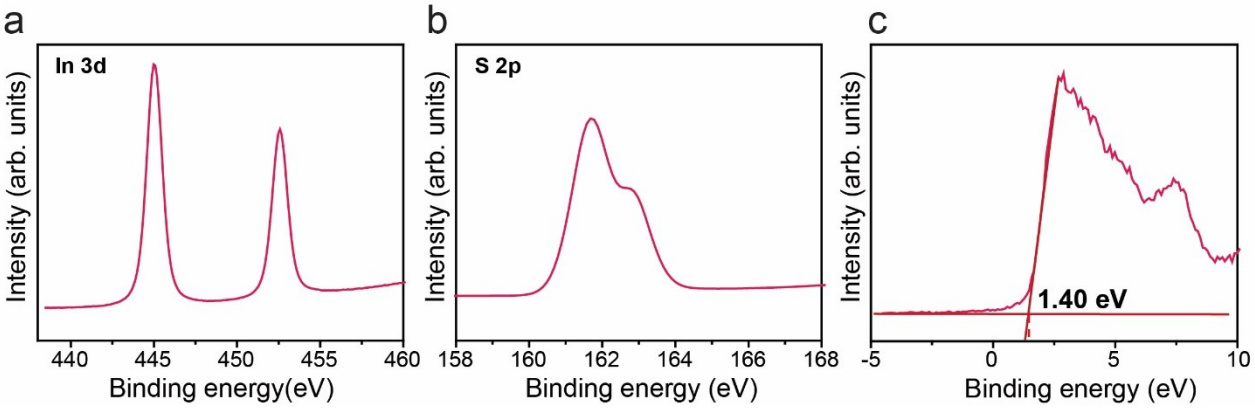

Fig. S5 X-ray photoelectron spectroscopy (XPS) spectra of (a) S*2p* and (b) In*3d* of the commercial In_2S_3 micro-sized powder. (c) XPS valance band spectrum revealing the energy difference of 1.40 eV between the valence band maximum (VBM) and Fermi level.

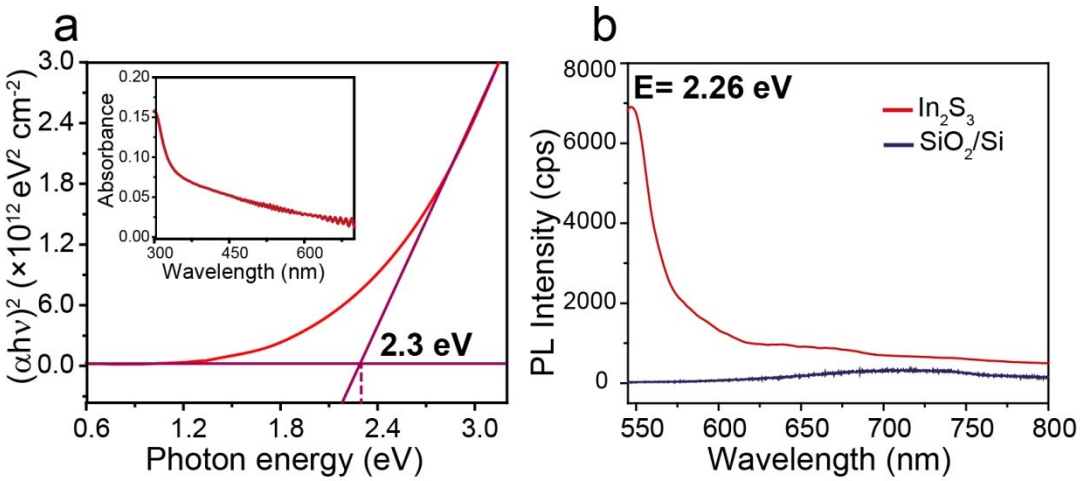

Fig. S6 (a) Tauc plot of an order-vacancy-enabled In_2S_3 layer derivate from UV-Vis-NIR absorption spectrum presented in the inset. The optical band gap is estimated to be ~2.3 eV. (b) The corresponding photoluminescence spectrum. The distinct peak at 548 nm indicates that the optical bandgap energy is ~2.3 eV.

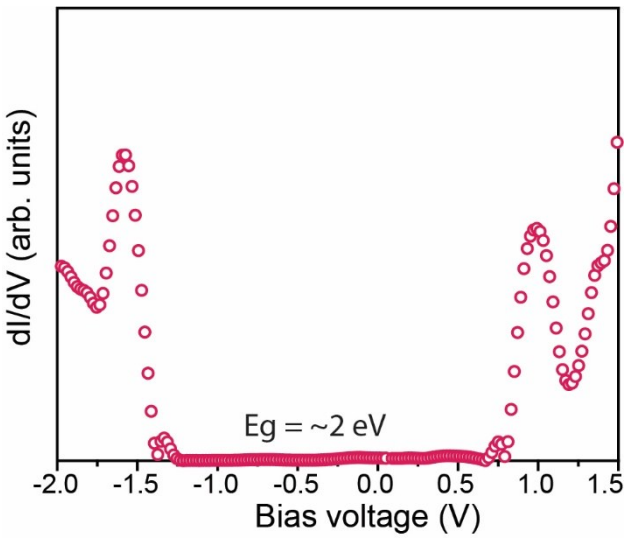

Fig. S7 The bandgap energy of ordered-vacancy In_2S_3 determined from the STM/STS measurements.

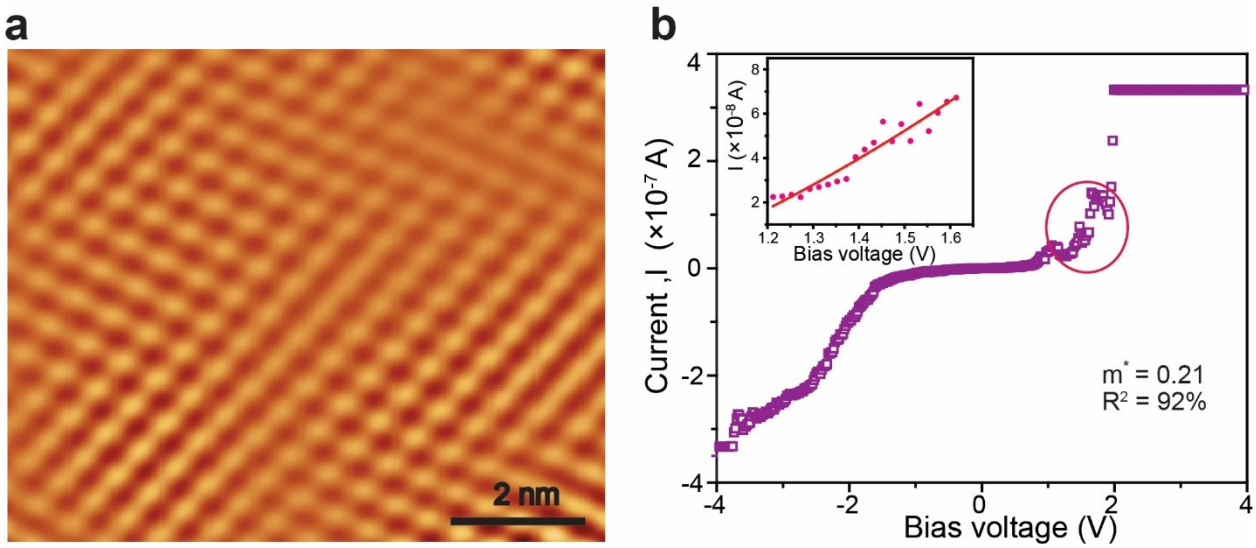

Fig. S8 (a) Scanning tunnelling microscopy/spectroscopy (STM/STS) image and (b) I-V Curve of In_2S_3 layer with ordered vacancies on the conductive silicon substrate measured at room temperature. The inset of graph b presents the Fowler-Nordheim tunnelling. The effective mass of electrons was estimated to 0.21 m* with R^2 of 0.92.

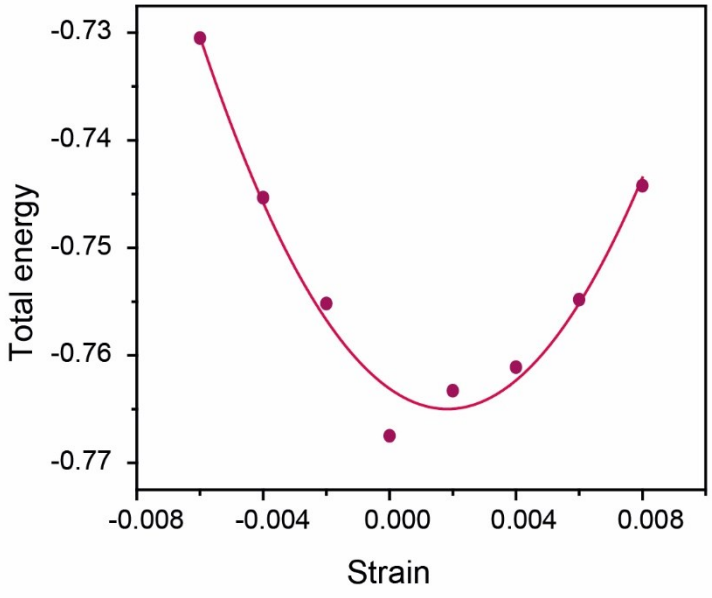

Fig. S9 The fitting of the band energy shift with respect to the strain variation of tetragonal In_2S_3 from the theoretical calculation.

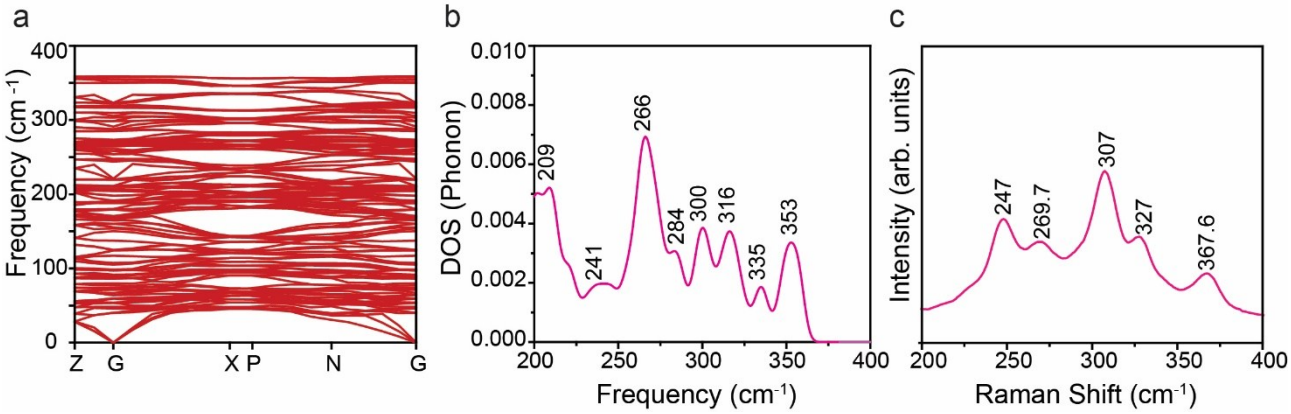

Fig. S10 (a) The calculated dispersion of phonon band of tetragonal In_2S_3. (b) The corresponding density of phonon states in the frequency range between 200 and 400 cm^{-1} extracted from the

dispersion of phonon band. (c) Raman spectrum of the In_2S_3 layer. The sample is obtained by multiple printing to gain sufficient signal.

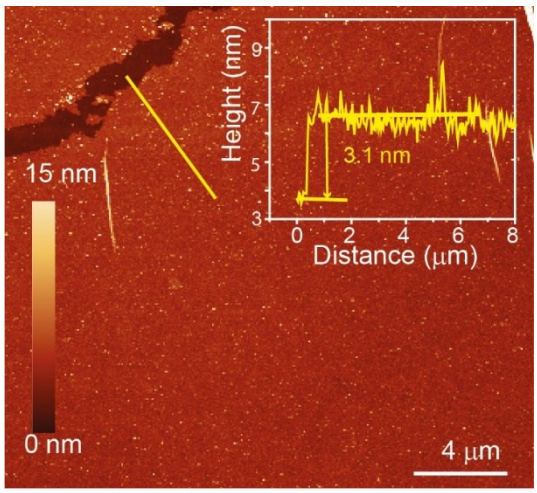

Fig. S11 AFM image of the In_2S_3 layer synthesised at 350°C with corresponding height profile (inset).

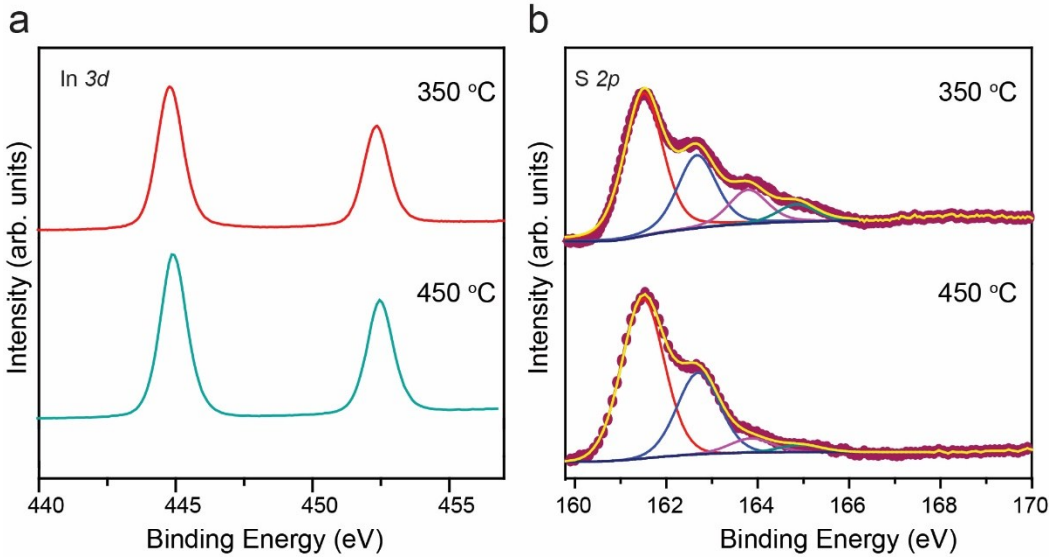

Fig. S12 Comparison of XPS spectra of (a) In*3d* and (b) S*2p* of the multiple printed In_2S_3 layer synthesised at 350 and 450°C.

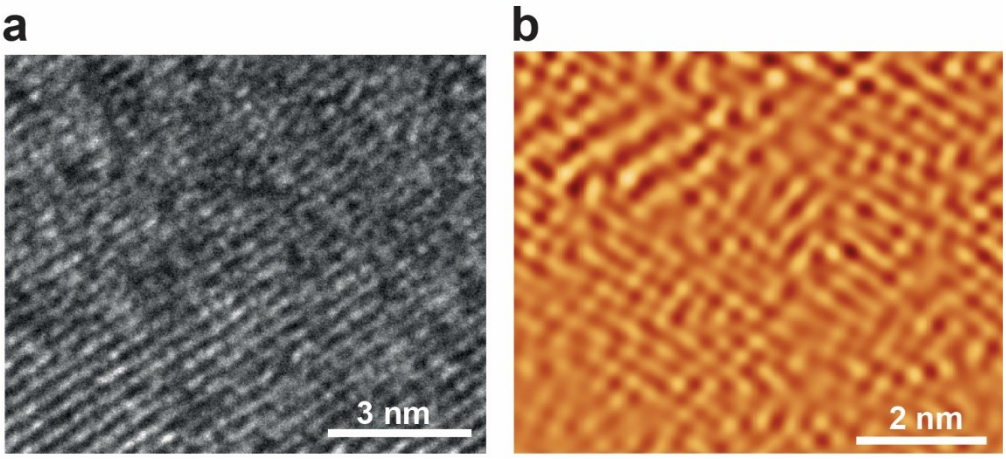

Fig. S13 (a) HRTEM and (b) STM images of In_2S_3 layer synthesised at 350°C.

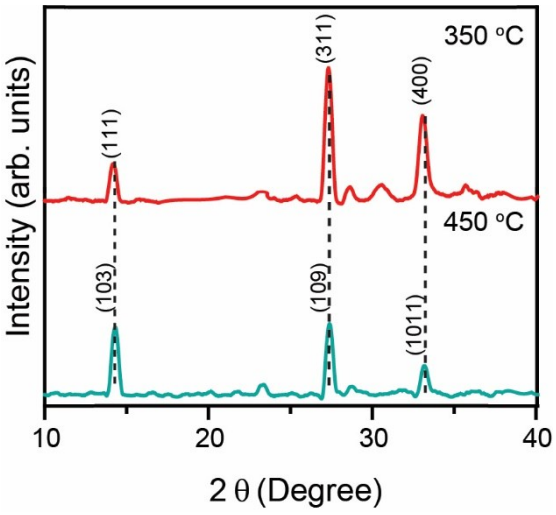

Fig. S14 XRD patterns of In_2S_3 layers synthesised at 350 and 450°C on glass substrates after multiple printing in order to gain sufficient signal.

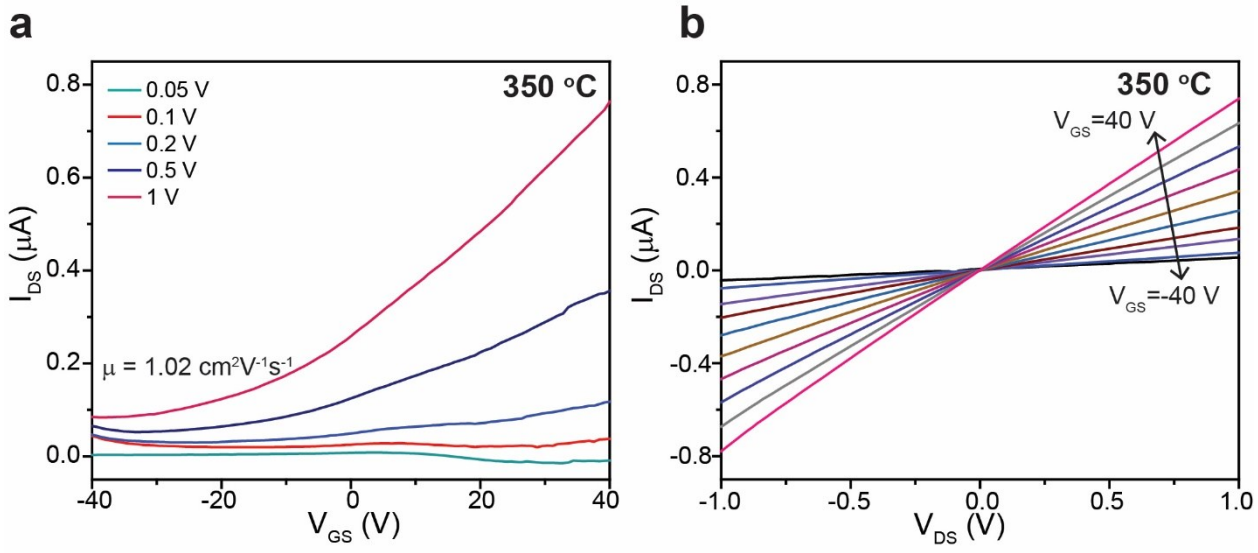

Fig. S15 (a) A typical source–drain current curve of a FET based on random-vacancy In_2S_3 layer synthesised at 350°C measured by altering the applied back-gate voltage for source–drain voltage varied from 0.05 to 1 V with channel length L = 9 μm and channel width W = 3 μm. the extracted field effect mobility is ~1.02 $cm^2V^{-1}s^{-1}$. (b) The current across drain and source (I_{DS}) for a device versus the drain-source voltage (V_{DS}) at different applied gate voltages (V_{GS}) ranged from –40 to 40 V of the corresponding device.

Note S1: The crystal growth direction of ordered-vacancy tetragonal In_2S_3

From the XRD pattern shown in Fig. S3a, the diffraction peaks at 14.2°, 27.4°, and 33.21° can be ascribed to the (103), (109), and (1011) crystallographic planes of tetragonal In_2S_3 (JCPDS Card No. 25-0390), respectively. This confirms the highly crystalline nature of the wafer-scale grown atomically-thin film and indicates the crystal growth direction is along the *a*- or *b*-axis. The high-resolution transmission electron microscopy (HRTEM) image in Fig. S3b shows a lattice spacing of

0.62 nm, corresponding to the (103) plane of tetragonal In_2S_3. The corresponding Fourier transform (FFT) pattern in Supplementary Fig. 3b further confirms the lateral growth direction.

Note S2: Measurement of effective electron mass for ordered vacancy enabled In_2S_3

The tunnelling current in which describe electrons tunnel from tip into the conduction band can be estimated and modelled using Fowler–Nordheim equation S1 as below[1]:

$$I_t \propto U^2 \exp\left(\frac{8\pi\sqrt{2m^*}}{3ehU}\varphi^{3/2}z\right) \quad \text{(S1)}$$

where I_t is tunneling current, U is bias voltage, m^* is effective mass of an electron, e is the charge of an electron, φ is the barrier height, z is the distance between tip and sample and h is Planck's constant. The proportionality is changed to equality incorporating a constant α_1. Further assuming constant φ and z during acquisition of an I-V curve, the equation S1 can be derived and simplified into the following equation to include constant α_2 [1].

$$I_t = \alpha_1 \times \mathrm{U}^2 \exp\left(\alpha_2 \frac{\sqrt{m^*}}{U}\right) \quad \text{(S2)}$$

Based on the STS I-V curve shown in Fig. S8 b, m^* is measured to be 0.21 m* with reliable coefficient, R^2 to be 0.92 through the fitting method as described in the experimental section.

Note S3: In_2S_3 with randomly distributed vacancies and its electrical performances

The decrease of sulphurisation temperature to 350°C does not change the thickness of printed In_2S_3 layer according to the AFM image shown in Fig. S11. In addition, XPS spectra in Fig. S12 show that the binding energies for In $3d_{5/2}$ and $3d_{3/2}$ peaks are similar to those of the 450°C sample. The S $2p_{3/2}$ and $2p_{1/2}$ peaks are observed at 161.6 and 162.6 eV, respectively for both 350 and 450°C samples [2-4]. Two additional S peaks are also seen at 163.8 and 164.8 eV, which are both ascribed to

the bridging S atoms [5, 6]. The high-resolution transmission electron microscopy (HRTEM) and scanning tunnelling microscopy (STM) images in Fig. S13 indicates the formation of defective surface for the 350°C sample. More importantly, according to the XRD patterns shown in Fig. S14, both peaks originally at 14.2° and 33.21° for the 450°C sample are slightly shifted to the left when lowering the sulphurisation temperature to 350°C, while the intensity ratio of the peak at 27.4° over that of 14.2° is significantly increased simultaneously. Such observation indicates that the highly defective structure leads to the crystal transformation from originally tetragonal enabled by ordered vacancies to cubic which is known to be stabilised by randomly distributed vacancies [7]. The disappearance of the ordered vacancy structure results in the dramatic reduction of the field effect electron mobility from ~56 to ~1 $cm^2V^{-1}S^{-1}$ (Fig. S15).

Table S1: **The calculated transport parameters of tetragonal In_2S_3**

Parameter	m^*/ m_0		C_{ij} (GPa)	E_d (eV)		μ_{xx} ($cm^2V^{-1}S^{-1}$)		τ (*fs*)	
	e	*h*	C_{11}	*e*	*h*	*e*	*H*	*e*	*h*
Values	0.153	23.14	48	13.6	4.5	1748	0.05	152	0.65

Where C_{11} refers to the elastic constant of the longitudinal acoustic wave along the transport directions, m^* is the effective mass, e is the electron carrier, h is hole carrier and the term E_d represents the deformation potential constant.

Table S2: **Comparison of the electrical performances of our FETs with those based on reported large-scale grown 2D metal chalcogenides**.

Materials	Method	Mobility ($cm^2V^{-1}s^{-1}$)	On/off ratio	Gate type	Gate oxide	Gate electrode	References
WS_2	ALD	3.9	NA	Top gate	HfO_2	Ti/Au	[8]
MoS_2	MOCVD	30	10^6	Top gate	HfO_2	Ti/Au	[9]
WS_2	MOCVD	18	NA	Top gate	HfO_2	Ti/Au	[9]
MoS_2	CVD	12.24	10^6	Back gate	SiO_2	Au	[10]
MoS_2	CVD	0.03	NA	Back gate	SiO_2	Ti/AU	[11]
GaS	vdW Exfoliation +CVD	0.2	150	Back gate	SiO_2	WS_2	[12]
MoS_2	CVD	0.04	NA	Back gate	SiO_2	Ti/Au	[13]
MoS_2	CVD	6	10^5	Back gate	SiO_2	Ti/Au	[13]
MoS_2	CVD	17	10^3	Back gate	SiO_2	Graphene	[14]
MoS_2	CVD	0.46	10^6	Back gate	SiO_2	Graphene	[15]
MoS_2	CVD	3.6	10^6	Back gate	SiO_2	Ti/Au	[16]
MoS_2	CVD	5.4	10^5	Back gate	SiO_2	Ti/Au	[17]
$MoTe_2$	PVD	10	10^5	Back gate	SiO_2	Pd	[18]
MoS_2	CVD	6	10^6	Back gate	SiO_2	Ti/Au	[19]
MoS_2	CVD	17.2	10^6	Top gate	ZrO_2	Graphene	[20]
In_2S_3	**vdW Exfoliation +CVD**	**58**	**10^4**	**Back gate**	**SiO_2**	**Cr/Au**	**This work**

References

1. L. Müller‐Meskamp, S. Karthäuser, H. J. Zandvliet, M. Homberger, U. Simon and R. Waser, *Small*, 2009, **5**, 496-502.
2. E. Kärber, K. Otto, A. Katerski, A. Mere and M. Krunks, *Mater. Sci. Semicond. Process.*, 2014, **25**, 137-142.
3. L.-Y. Chen, Z.-D. Zhang and W.-Z. Wang, *J. Phys. Chem. C*, 2008, **112**, 4117-4123.
4. W. Huang, L. Gan, H. Yang, N. Zhou, R. Wang, W. Wu, H. Li, Y. Ma, H. Zeng and T. Zhai, *Adv. Funct. Mater.*, 2017, **27**, 1702448.
5. O. A. Carrasco-Jaim, R. Ahumada-Lazo, P. C. Clark, C. Gómez-Solis, S. M. Fairclough, S. J. Haigh, M. A. Leontiadou, K. Handrup, L. M. Torres-Martínez and W. R. Flavell, *Int. J. Hydrog. Energy*, 2019, **44**, 2770-2783.

6. H. Lin, L. Yang, X. Jiang, G. Li, T. Zhang, Q. Yao, G. W. Zheng and J. Y. Lee, *Energ. Environ. Sci.*, 2017, **10**, 1476-1486.
7. P. Pistor, J. M. Merino Álvarez, M. León, M. Di Michiel, S. Schorr, R. Klenk and S. Lehmann, *Acta Crystallogr. B*, 2016, **72**, 410-415.
8. K. Kang, S. Xie, L. Huang, Y. Han, P. Y. Huang, K. F. Mak, C.-J. Kim, D. Muller and J. Park, *Nature*, 2015, **520**, 656.
9. J. Park, N. Choudhary, J. Smith, G. Lee, M. Kim and W. Choi, *Appl. Phys. Lett.*, 2015, **106**, 012104.
10. Y. Yu, C. Li, Y. Liu, L. Su, Y. Zhang and L. Cao, *Sci. Rep.*, 2013, **3**, 1866.
11. Y. H. Lee, X. Q. Zhang, W. Zhang, M. T. Chang, C. T. Lin, K. D. Chang, Y. C. Yu, J. T. W. Wang, C. S. Chang and L. J. Li, *Adv. Mater.*, 2012, **24**, 2320-2325.
12. B. J. Carey, J. Z. Ou, R. M. Clark, K. J. Berean, A. Zavabeti, A. S. Chesman, S. P. Russo, D. W. Lau, Z.-Q. Xu and Q. Bao, *Nat. Commun.*, 2017, **8**, 14482.
13. Y. Zhan, Z. Liu, S. Najmaei, P. M. Ajayan and J. Lou, *Small*, 2012, **8**, 966-971.
14. L. Yu, Y.-H. Lee, X. Ling, E. J. G. Santos, Y. C. Shin, Y. Lin, M. Dubey, E. Kaxiras, J. Kong, H. Wang and T. Palacios, *Nano Lett.*, 2014, **14**, 3055-3063.
15. S. Baroni, S. De Gironcoli, A. Dal Corso and P. Giannozzi, *Rev. Mod. Phys.*, 2001, **73**, 515.
16. R. Kappera, *APL Mater.*, 2014, **2**, 092516.
17. J.-G. Song, J. Park, W. Lee, T. Choi, H. Jung, C. W. Lee, S.-H. Hwang, J. M. Myoung, J.-H. Jung and S.-H. Kim, *ACS nano*, 2013, **7**, 11333-11340.
18. X. Chen, Y. J. Park, T. Das, H. Jang, J.-B. Lee and J.-H. Ahn, *Nanoscale*, 2016, **8**, 15181-15188.
19. Z. Dai, Z. Wang, X. He, X.-X. Zhang and H. N. Alshareef, *Adv. Funct. Mater.*, 2017, **27**, 1703119.
20. M. Zhao, Y. Ye, Y. Han, Y. Xia, H. Zhu, S. Wang, Y. Wang, D. A. Muller and X. Zhang, *Nat. Nanotechnol.*, 2016, **11**, 954.